Deformation microstructure and tensile properties of Alloy 709 at different temperatures

Ding, Rengen; Yan, Jin; Li, Hangyue; Yu, Suyang; Rabiei, Afsaneh; Bowen, Paul

DOI:
10.1016/j.matdes.2019.107843

Document Version
Publisher's PDF, also known as Version of record

Citation for published version (Harvard):
Ding, R, Yan, J, Li, H, Yu, S, Rabiei, A & Bowen, P 2019, 'Deformation microstructure and tensile properties of Alloy 709 at different temperatures', *Materials and Design*, vol. 176, 107843, pp. 107843. https://doi.org/10.1016/j.matdes.2019.107843

Materials and Design 176 (2019) 107843

Contents lists available at ScienceDirect

Materials and Design

journal homepage: www.elsevier.com/locate/matdes

Deformation microstructure and tensile properties of Alloy 709 at different temperatures

Rengen Ding [a,*], Jin Yan [a], Hangyue Li [a], Suyang Yu [a], Afsaneh Rabiei [b], Paul Bowen [a]

[a] School of Metallurgy and Materials, University of Birmingham, Edgbaston, Birmingham B15 2TT, UK
[b] Department of Mechanical and Aerospace Engineering, North Carolina State University, 911 Oval Dr, Raleigh, NC 27695-7910, USA

HIGHLIGHTS

- DSA effect was observed at 550°C in both as-received and aged materials.
- Yield strength of the as-received alloy reduces with increasing temperature but no clear reduction in range of 550-750°C.
- Aging increases the yield strength but reduces the ultimate tensile strength and ductility.

GRAPHICAL ABSTRACT

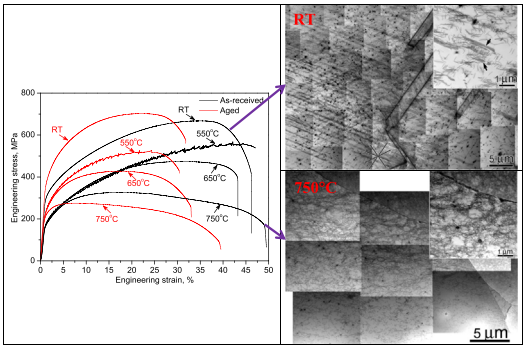

ARTICLE INFO

Article history:
Received 7 March 2019
Received in revised form 29 April 2019
Accepted 8 May 2019
Available online 9 May 2019

Keywords:
Alloy 709
Tensile
Microstructure
TEM

ABSTRACT

Alloy 709 austenitic stainless steel is being investigated as a candidate structural material for the next generation fast neutron reactors at service temperature of 500–550 °C. However, the study of deformation mechanisms on Alloy 709 and of tensile response of aged Alloy 709 is lacking. In this study, thus, the tensile behaviour of as-received and aged Alloy 709, their deformation microstructures and failure mechanisms, have been investigated at room temperature (RT), 550, 650 and 750 °C. Aging brought about the formation of particles at grain boundaries and interior of grain, thus leading to enhancement of yield strength but reduction in ductility. The ultimate strength of both materials is strongly temperature dependent, which clearly decreases with temperature. It is caused by the decreasing strain hardening ability, dynamic strain aging and dynamic recovery together with dynamic recrystallisation at different temperatures.

1. Introduction

Austenitic stainless steels are the most widely used stainless steels. Due to excellent corrosion resistance and mechanical properties at high temperatures, they are used in a wide variety of aerospace, powerplant and chemical applications. To meet continuous increasing service temperature, advanced heat-resistant austenitic stainless steels with complex chemical compositions, such as HR3C (Sumitomo Metal, Japan), Sanicro 25 (Sandvik, Sweden), DMV 310N (Salzgitter, Mannesmann, Germany) and NF709/Alloy 709 (Nippon Steel, Japan) have been developed. NF709 was developed based on Nb/Ti stabilized 20Cr25Ni stainless steel. Alloy 709 is similar in chemical composition

* Corresponding author.
E-mail address: r.ding@bham.ac.uk (R. Ding).

https://doi.org/10.1016/j.matdes.2019.107843

to NF709 but without Ti. Currently, Alloy 709 is regarded as one of the best austenitic steels for elevated temperature applications because of its creep and corrosion resistance and is being investigated as a candidate structural material for the next generation fast neutron reactors. The operating temperature of the fast neutron reactors will be increased to 500–550 °C as liquid sodium is used in the primary and secondary thermal circulation. As a candidate structural material used in the neutron reactors, the mechanical properties at elevated temperature, such as high temperature strength, creep strength, ductility and fatigue crack growth resistance, are of vital importance. Very recently, Alomari et al. [1] studied tensile behaviour of this alloy from room temperature to 800 °C. They found that stress-strain curves show serrations known as Portevin-Le Chatelier effect (PLE) at temperatures from 250 to 650 °C at a strain of 10^{-4}/s. The phenomenon is usually attributed to a macroscopic observation of dynamic strain aging (DSA) resulting from interaction between solute atoms and moving dislocations during deformation. They also noted that, contrary to the commonly observed embrittlement during DSA, a distinct enhancement in ductility was observed. In-situ scanning electron microscopy along with loading and heating of this alloy at temperatures up to 950 °C has also reported stress-strain curves with serrations at temperatures from 550 to 800 °C [2]. The authors also investigated fatigue crack growth resistance of the Alloy 709 at elevated temperatures, and found that the crack growth rate is faster in air than in vacuum but less sensitive to temperature in vacuum than in air [3]. These studies have enhanced understanding of the mechanical properties of this alloy at high temperature. It is well known that the mechanical responses of the materials are associated with its deformation behaviours. However, the study of deformation mechanisms on the alloy 709 is lacking in open literature. As such, this has become one of the aims of the current study. In the other austenitic stainless steels, particularly on 316, the deformation mechanism has been widely studied. Byun et al. [4] investigated the deformation mechanisms of 316LN austenitic stainless steel and found that dislocations are unable to cross-slip when the test temperature is below 200 °C, leading to formation of large dislocation pile-ups below 200 °C but tangled dislocations above 200 °C. Pei et al. [5] noted that the 316LN is deformed via dislocation sliding and twining at 400 °C or below, dislocation cross-slipping at 600 °C, dynamic recovery at 700 °C and dynamic recrystallization at 800 °C or above. In 316 austenitic stainless steel, Michel et al. [6] found that dislocation cell walls are formed via tangled dislocations below ~$0.5T_m$ while regular sub-boundaries are developed above ~$0.5T_m$. Based on previous studies, the deformation mechanisms of austenitic steels depend on the temperature and chemical composition [7–9]. In this study, the deformation behaviour of the Alloy 709 will be compared to that of 316 steel and any potential similarity or differences will be reported.

Unlike conventional solid solution austenitic stainless steels, the advanced austenitic stainless steels, such as NF709 and Alloy 709, develop a variety of precipitates during aging at different temperatures which leads to good mechanical properties at high service temperatures. Sourmail and Bhadeshia [10] investigated precipitation behaviour of NF709 at 750 and 800 °C, and found that $M_{23}C_6$ (after short aging) and Cr_3Ni_2SiX(X: mainly N) (after long aging) precipitated at grain boundaries and twin boundaries, together with the formation of *Z*-phase (CrNbN) predominately on dislocations. Such microstructural evolution could directly impact the mechanical (e.g. tensile) properties of the material. The study on the effect of aging on tensile properties is, therefore, of practical importance for the application of the Alloy 709 in the fast neutron reactors.

Thus, in this study, to investigate the influence of aging on the tensile behaviour of Alloy 709, the as-received material was aged at 650 °C for 2000 h and then tensile tests were conducted at various temperatures on both as-received and aged samples. Their deformation microstructure was analysed using transmission electron microscopy (TEM). Variation in the tensile behaviours with temperature is discussed based on microstructural evolution.

2. Material and experimental procedures

The Alloy 709 used in this study was fabricated using vacuum-induction melting (VIM) and electro-slag remelting (ESR) processes by Carpenter Technologies. Ingot from the VIM was homogenized at 1250 °C for 4 h, hot forged at 1100 °C and then rolled at 1100 °C. The hot-rolled plate was finally annealed at 1100 °C for 2 h, followed by water quenching. The nominal chemical composition of the material provided by the manufacturer is shown in Table 1.

In order to investigate the effect of aging on tensile properties of the Alloy 709, the as-received block was aged at 650 °C for 2000 h in a vacuum furnace to simulate microstructure evolution during service. Tensile samples with a gage section diameter of 5 mm and a reduced section length of 25.3 mm were machined from the as-received and aged materials. The tensile tests were conducted using a Zwick mechanical testing machine at room temperature, 550, 650 and 750 °C in air under a nominal strain rate of 1×10^{-4}/s. The temperature was maintained within ±2 °C and the soaking time for each sample was kept at 30 min for test at each temperature. To study the effect of temperature on deformation mechanism, some tests were interrupted at a nominal strain of ~2%. This means that the testing time for the interrupted samples is ~3 min. Thus, the total time for the interrupted samples is about 33 min at the target temperatures. The strain-hardening of the Alloy 709 was analysed. A standard approach [11] was adopted for measuring stress values from the stress-strain curves showing serrated flow.

To understand the influence of precipitates induced by aging on the mechanical behaviour and plastic deformations, microstructure including precipitates was investigated using TEM before and after tensile test. The discs with 3 mm in diameter were cut perpendicularly from the gauge length of the tensile samples, and then mechanically ground to 100 μm in thickens, followed by electropolishing in a solution of 10% perchloric acid +90% ethanol at 20 V and −20 °C. TEM observation was carried out on a FEI Talos F200X microscope equipped with Super-X energy dispersive X-ray spectroscope (EDS) operating at 200 kV.

In order to explore fracture mechanism, longitudinal sections of fractured testpieces and fracture surfaces were examined on FEI Quanta 3D and Helios dual-beam scanning electron microscopes (SEM). Grain size was measured using Oxford Instruments Nordlys EBSD (electron backscatter diffraction) detector with step size of 1 μm for the as-received material. To reveal the formation of subgrains during tension testing, however, the step size of 50 nm was used in the sectioned samples.

3. Results and analysis

3.1. Initial microstructure of the as-received and aged materials

Fig. 1 exhibits EBSD mapping from the as-received material, showing that the Alloy 709 has average grain size of ~48 μm and that ~45% of boundaries are Σ3 twin boundaries. No evidence of strong texture was found in the as-received samples (Fig. 1d), suggesting that annealing efficiently alleviated the texture produced by rolling. A typical backscattered electron (BSE) image (Fig. 2) shows the band-like distribution of the white particles. EDS analysis indicates that these white particles are Nb-rich carbonitride (i.e. Nb(C,N)) (Fig. 2). Such large Nb(C,N) could be formed during casting, and then broke down and aligned along the rolling direction during rolling process. Thus, this type of the carbonitrides with sizes in the range of 1–10 μm is referred to as primary Nb(C,N). A considerable number of nano-sized particles are also observed, as shown in

Table 1
Chemical composition of the Alloy 709 (wt%).

Ni	Cr	Nb	Mn	Mo	N	Si	B	C	S	Ti	Fe
25.01	19.89	0.25	0.90	1.51	0.14	0.39	0.0037	0.078	0.0006	<0.01	Balance

Fig. 3. EDS mapping indicates that they are also Nb carbonitrides (Fig. 3). The analysis of convergent beam electron diffraction (CBED) patterns from a Nb carbonitride suggests that such particle has fcc structure with lattice parameter a = 0.44 nm (Fig. 3). Such fine particles could precipitate during cooling after solidification and annealing. It should be noted that some dislocations with relatively low density were also observed, which could be induced by water quenching.

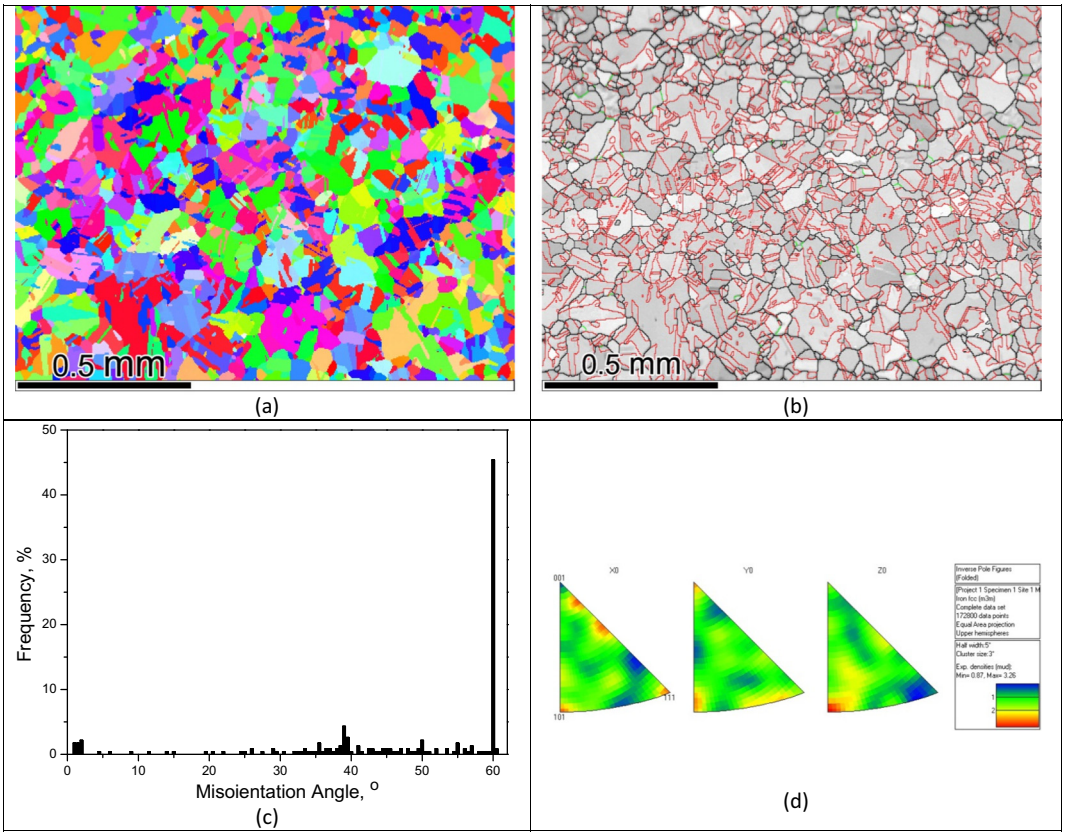

Fig. 1. Microstructure of as received Alloy 709 with: EBSD orientation map (a), grain and twin boundaries (b), the corresponding misorientation angle distribution (c), and inverse pole figure (d). Note: in (b), dark-line: >15°, green-line: <5° and red-line: Σ3 twin boundaries.

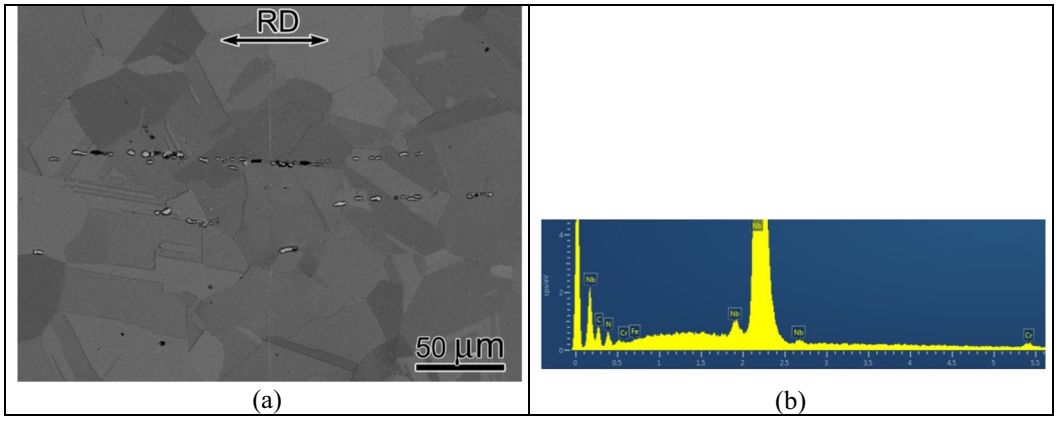

Fig. 2. A typical SEM- BSE image of as-received Alloy 709, showing the band-like distribution of the white particles (a), EDS spectrum indicates that those white particles could be Nb-rich carbonitride (b). Note: RD – rolling direction.

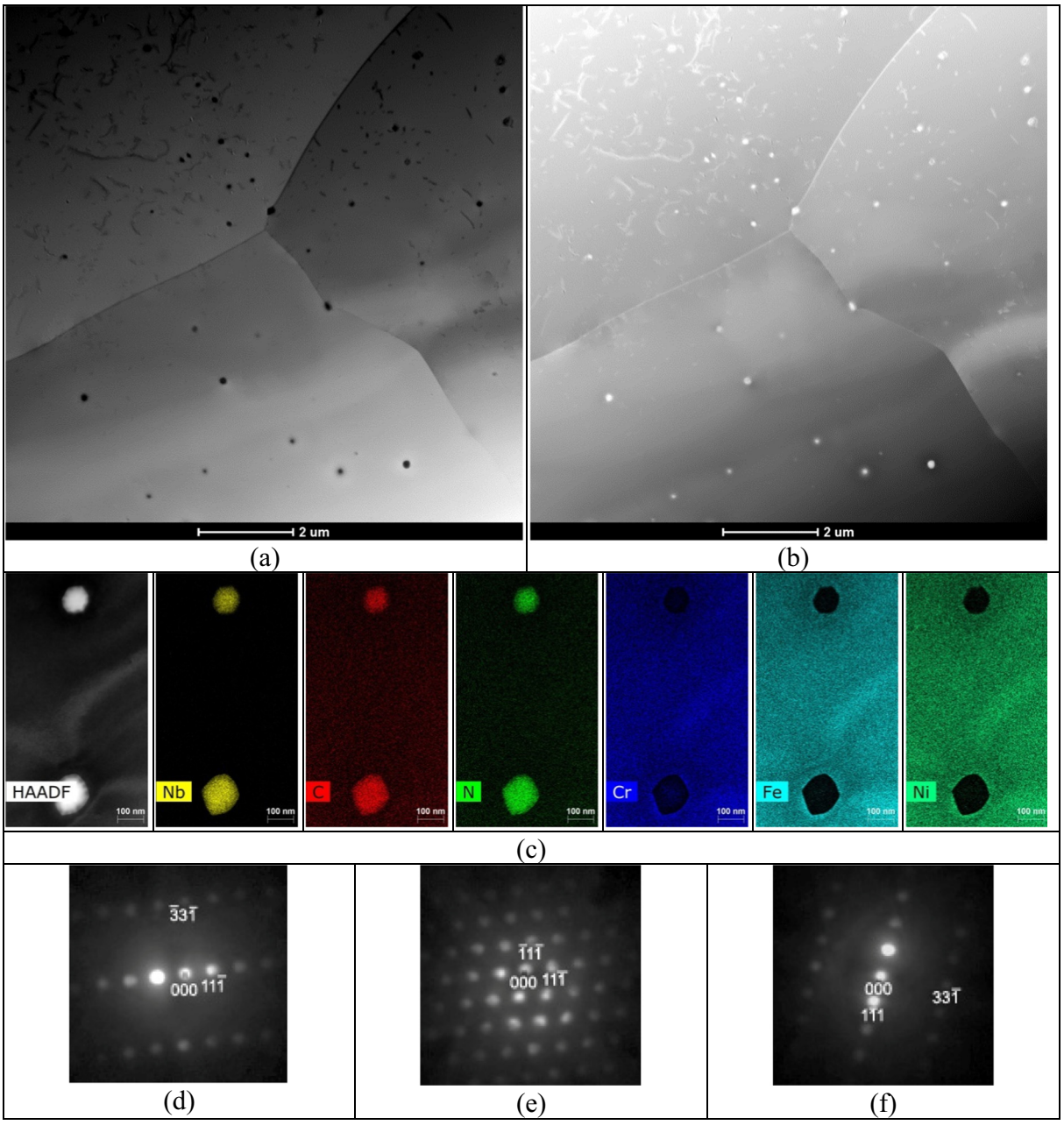

Fig. 3. Bright field (BF) scanning transmission electron microscopy (STEM) image (a) and high angle annular dark field (HAADF) STEM image (b) of the as-received material show nano-sized precipitates, EDS mapping suggests that these particles are Nb carbonitrides (c), three convergent beam electron diffraction patterns recorded along [123] (d), [011] (e) and [−123] (f) from a Nb (CN).

Fig. 4 shows the microstructure of the sample that is aged at 650 °C for 2000 h. As can be seen, aging has promoted the formation of globular particles on grain boundaries and the interior of grains (Fig. 4). EDS mapping suggests that most of these particles are (Cr,Mo)-rich carbide (i.e. $M_{23}C_6$) and often they appear as composite particles with a Nb(C, N) core and a shell of $M_{23}C_6$ (Fig. 4). It should be noted here that some particles are (Cr,Ni,Mo,Si)-rich nitrides (Fig. 4), designated as θ phase. A large number of the particles of several nanometers size precipitated on dislocations, which based on EDS analysis they are identified as Z phase (NbCrN) (Fig. 5). A complete report with detailed explanation of the microstructure and all different types of precipitations and phases present in as-received and aged samples of Alloy 709 can be found elsewhere [12]. A continuous distribution of the particles at grain boundary and a large amount of the particles (especially for Z-phase) precipitating on the interior of grains, will inevitably affect the mechanical response of Alloy 709.

3.2. Tensile properties

Typical engineering stress - strain curves of the as-received and aged samples at various temperatures are shown in Fig. 6. As can be seen, Alloy 709 shows serrated flow during tensile deformation at intermediate temperatures depending on heat treatment (Fig. 6b). For example, the as-received sample shows serration at 650 °C while the aged sample does not exhibit serration at the same temperature. At 550 °C, the serrated flow commences after a critical strain (e.g. 1.6% for as-received sample) and continues until fracture occurs but it only occurs at strains ranging from 1.2% to 2.5% at 650 °C for the as-received sample. The

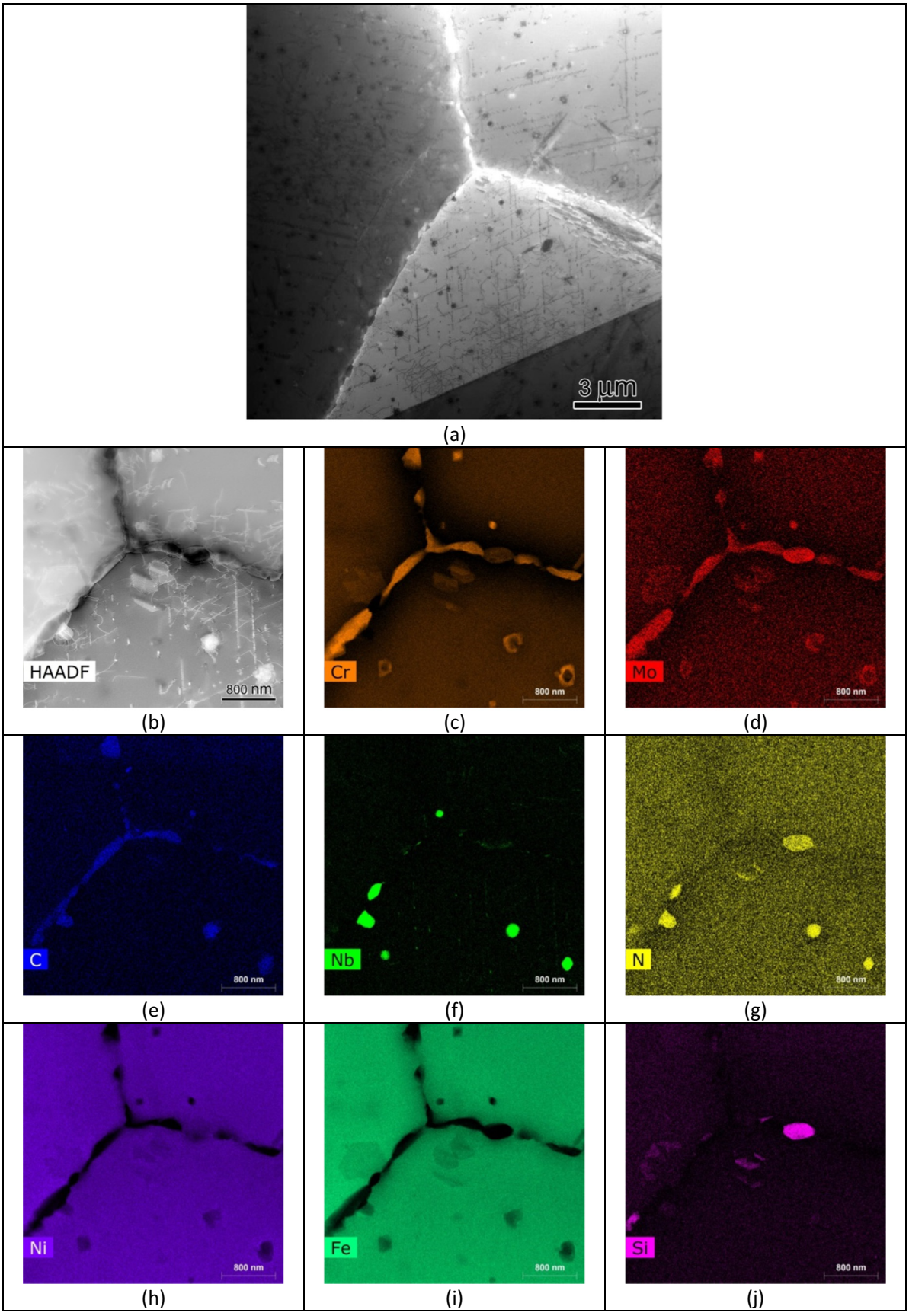

Fig. 4. BF (a) and HAADF (b) STEM images of aged material shows that the globular particles nearly continuously distributed on grain boundaries, higher magnification image of Fig. 4a exhibits EDS mapping region (b), EDS maps (c–j) reveal that most of grain boundary (GB) particles are (Cr,Mo)-rich carbide ($M_{23}C_6$), while most of particles precipitated at the interior of grains have a Nb(C,N) core with $M_{23}C_6$ shell.

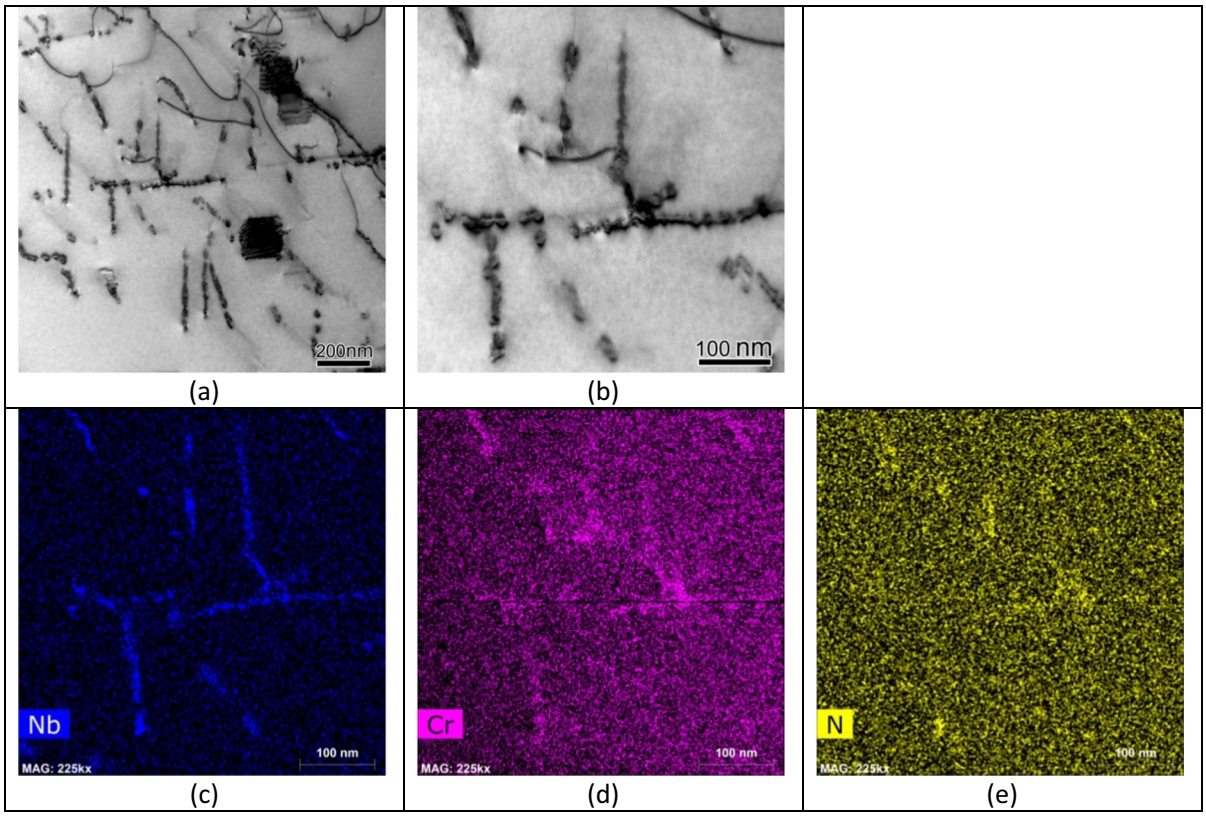

Fig. 5. BF-STEM images show that a large number of ~10 nm particles precipitate on dislocations (a and b), higher magnification image of (a) shows EDS mapping area (b), EDS maps of Nb (c), Cr (d) and N (e) suggest that those nano-sized particles are (Nb,Cr)-rich nitrides (i.e. Z phase).

occurrence of serrated flow is attributed to DSA effect, which is generally believed to be caused by pining or unpinning processes between interstitials/solute atoms and mobile dislocations [13–15]. Additionally, Suzuki segregation can also play an important role in the DSA effect due to interactions between solute atoms and stacking faults [16,17]. It is known that at low temperatures, the interstitials/solute atoms are immobile with respect to the moving dislocations and thus could not impede dislocation motion [18]. At high temperatures, the mobility of solute atoms is high enough to follow the dislocations without any drag or disruption [18]. Very recently, Alomari et al. [1] reported that the DSA regime of Alloy 709 to be within 250–650 °C at a strain of 10^{-4}/s, which is consistent with the observations reported for various austenitic stainless steels [19]. For instance, Choudhary et al. suggested that DSA in a type of 316 LN stainless steel is caused by the diffusion of interstitials (C + N) in the low temperature regime (250–325 °C) and by substitutional solutes in the high temperature regime (400–600 °C) [19].

The variations of 0.2% offset yield strength (YS) and the ultimate tensile strength (UTS) of the two investigated materials (as-received and aged Alloy 709) with temperature are illustrated in Fig. 7a. As can be seen, the as-received material shows ~300 MPa YS at room temperature. The yield strength reduces to ~200 MPa at 550 °C but does not decrease significantly with further increasing of temperature. However, the UTS decreases consistently with increasing testing temperature. The aged material shows higher yield stress and lower UTS but has a similar variation with testing temperature to the as-received material. This means that aging leads to reduction in ductility, as shown in Fig. 7b. Temperature effect on ductility of this alloy can be defined as a function of the elongation-to-fracture, ε_f, uniform elongation, ε_u (i.e. elongation up to maximum stress in a true stress-strain curve) and non-uniform elongation, ε_{nu} (i.e. post-uniform elongation or necking strain, or $\varepsilon_{nu} = \varepsilon_f - \varepsilon_u$). The ε_{nu} for the as-received material at 550 °C is close to zero (Fig. 7b), which means that almost no necking occurs. Aging enhances non-uniform elongation of the Alloy 709 at elevated temperatures (Fig. 7b).

The stress-strain curves (Fig. 6) indicate that the strain-hardening rate ($d\sigma/d\varepsilon$) could be related to testing temperature and aging. Fig. 8 shows such temperature and aging dependence of the strain-hardening rate of Alloy 709. As can be seen, all samples exhibit a steep decrease in strain-hardening rate when strains are below 2%, corresponding to the elastic-plastic transition. At room temperature, the strain-hardening rate of the as-received sample decreases slightly with strain after the elastic-plastic transition, from an initial of ~3000 MPa to ~800 MPa at a strain of 31%. It is interesting that Alloy 709 at 550 °C shows higher strain-hardening rate than that at RT after elastic-plastic transition, and still keeps ~2000 MPa strain-hardening rate even at a strain of ~30%. Another interesting observation is that, at 650 °C, the strain-hardening rate shows a small peak where its rate is the same as that at RT until a strain of ~2.5%. Both interesting observations propose that their high strain hardening rates may result from DSA effect. The strain-hardening rate drops faster with testing at 750 °C. Compared with the as-received samples, the aged samples show higher strain-hardening rate at early stage of plastic deformation, followed by lower rate. For instance, as strain is below 9%, the aged sample exhibits higher strain-hardening rate than the as-received sample at RT. These findings including DSA, suggest that deformation mechanisms of the Alloy 709 could vary with temperature and aging. Thus, deformation structures are examined via TEM on the interrupted samples at ~2% strain (which is within DSA regime) as well as the failed tensile samples. The results are given in the next section of this report.

3.3. Deformation microstructure at different temperatures

The microstructures of the interrupted as-received samples at various testing temperatures are illustrated in Fig. 9. The BF-STEM image

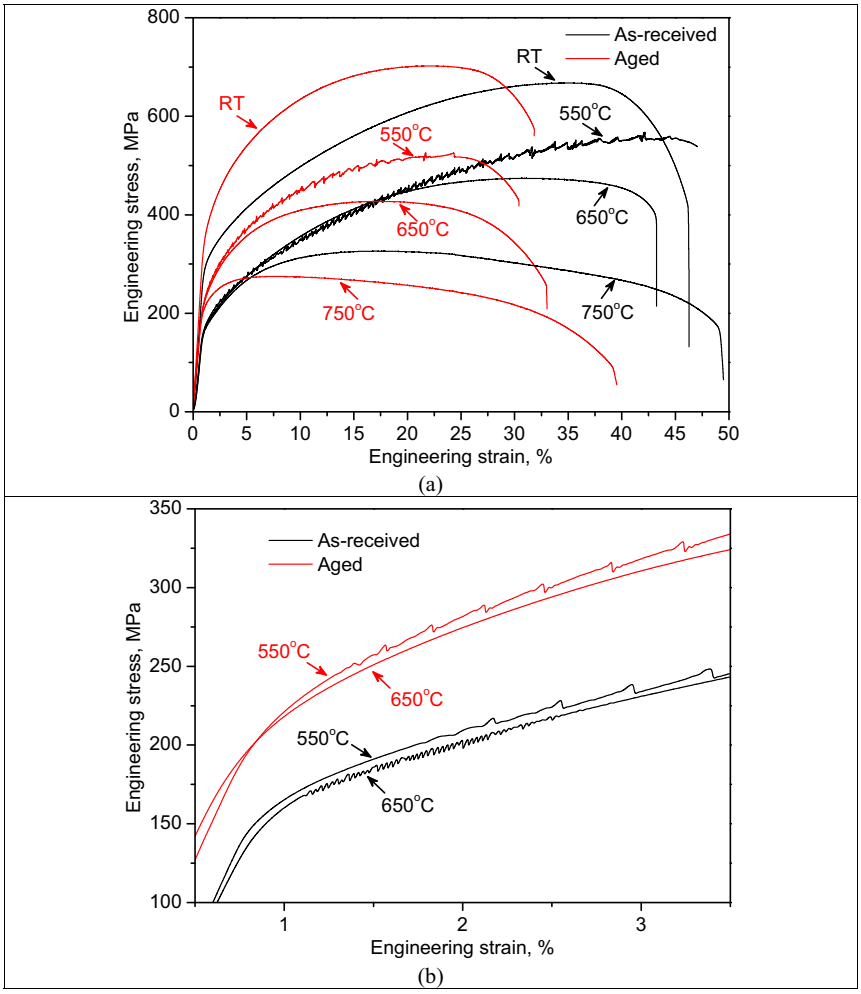

Fig. 6. Engineering stress – strain curves for the as-received and aged samples at different temperatures (a), and zoom in segment of Fig. 6a within the early stage of plastic deformation (b) exhibits the serrated flows at intermediate temperatures (550° and 650 °C).

taken from the as-received sample at RT using multi-beam condition with beam direction of ~[101] is shown in Fig. 9a, where the dislocations are well-definitely arranged on $(\bar{1}11)$ and $(11\bar{1})$ planes (edge on) and on $(1\bar{1}1)$ and (111) planes (incline to the image). This suggests that the as-received sample is deformed predominantly via dislocation slip on {111} planes with some stacking fault ribs (arrowed in inset of Fig. 9a). The distribution of dislocations in the as-received samples is relatively uniform. Compared to the sample tested at RT, a considerable number of slip bands and stacking fault ribs are observed at 550 °C (Fig. 9b). A microstructure similar to that in the sample tested at 550 °C is also observed in the sample tested at 650 °C (Fig. 9c). In other words, at both 550 and 650 °C, the alloy is deformed mainly via planar slip and stacking faults. However, in the sample tested at 750 °C, dislocations tangled together and dislocation cells start to form as a result of the arrangement of dislocations (Fig. 9d). It should be noted that, Fig. 9d was also recorded using beam direction of ~[101], however none of the linear dislocation substructure that was observed at lower temperatures could be found at 750 °C. This indicates that at 750 °C the cross-slip of dislocations and probably climb must occur frequently. The observed linear dislocation substructure is pronounced as a manifestation of deformation by planar slip of dislocations restricting the cross-slip and recovery due to DSA at intermediate temperatures (550 and 650 °C here) [20].

Fig. 10 shows BF-STEM images taken from the as-received samples strained to failure at various temperatures. At room temperature, the deformation microstructures exhibit band-like features (Fig. 10a) and dense tangled dislocations start to form dislocation cells (Fig. 10b). In the tensile sample at 550 °C, intensive band-like features are observed, as shown in Fig. 10c. This indicates that significant strain localisations took place, which will lead to shear fracture. At 650 °C the deformation microstructures consist of dislocation cells (Fig. 10d) along with some dislocation walls (Fig. 10e). The microstructure of the sample tested at 750 °C composes of considerable amounts of subgrains with sizes in the range of submicron to 1 μm and of some elongated dislocation cells (Fig. 10f). Meanwhile, the dislocation density decreases remarkably at 750 °C. Those subgrains prominently locate close to the grain boundaries (arrowed), which is also confirmed by EBSD map shown in Fig. 11.

In order to understand why aging enhances necking strain (ε_{nu}) of the Alloy 709 at elevated temperatures (Fig. 7b), deformation microstructure of the aged samples strained to failure was also examined. The main difference in deformation microstructure between the as-received and aged samples is: 1) some subgrains were observed at 650 °C in the aged sample (Fig. 12a), 2) more subgrains were found in the aged sample tested at 750 °C (Fig. 12b). This suggests that aging may promote recovery and dynamic recrystallization (DRX), thus leading to the higher necking strains observed in the aged samples at elevated temperatures. In other words, this promotion of DRX is attributed to the effect of precipitates produced by aging. The influence of precipitates on DRX can be summarised as: 1) the stored energy of plastically deformed fcc alloys having second phase particles is higher than that of the same alloys without particles [21], which promotes

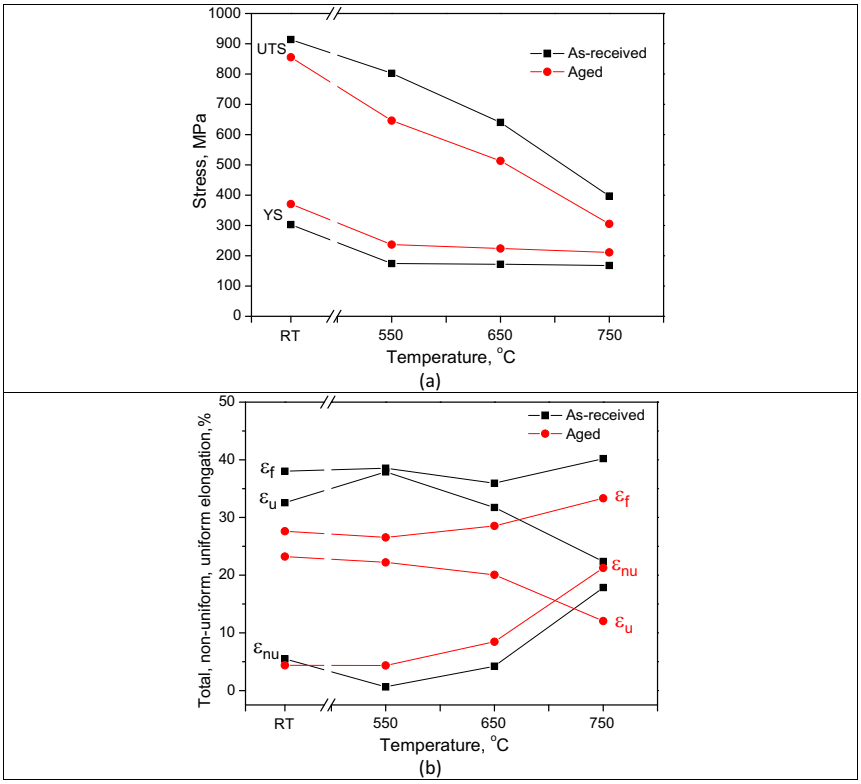

Fig. 7. Effect of test temperature on yield (YS) and ultimate tensile strengths (UTS) (a) as well as ductility (ε_f), uniform (ε_u) and non-uniform (ε_{nu}) elongations (b).

the initial stage of DRX; 2) large particles may simulate DRX nucleation site (arrowed in dark in Fig. 12c) due to higher deformation heterogeneities around these particles [22]; and 3) closely spaced particles exert substantial pinning force on the mobility of low angle and high angle boundaries as well as dislocations [23]. The first two factors enhance recrystallization process whereas the last one retards recrystallisation. In this study, however, the synergetic effect is that precipitates produced by aging promote DRX.

3.4. Formation of precipitates and elemental segregation at grain boundary in the as-received alloy during tensile test

As mentioned in Section 3.1, the precipitates in the as-received alloy involve only primary Nb(C,N) with size of up to a few microns

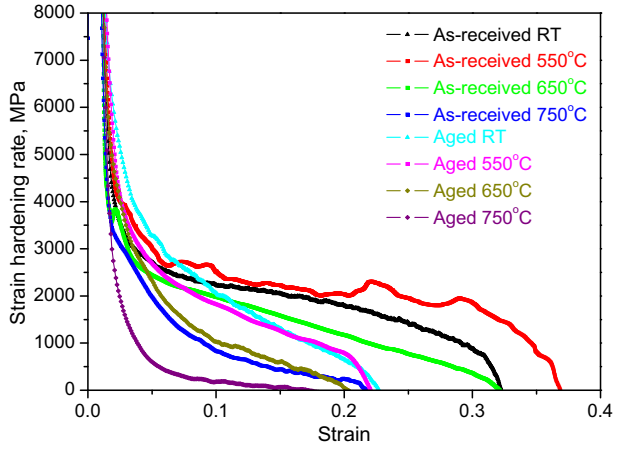

Fig. 8. Temperature dependence of the strain-hardening rate in the as-received and aged Alloy 709.

and nano-sized Nb(C,N). However, the tensile testing at elevated temperatures may promote the formation of new particles and segregation of solute elements at grain boundary, which could influence mechanical responses of the Alloy 709. This investigation could, thus, be beneficial to explain variation in mechanical behaviours at different temperatures. TEM examination shows almost no change in Nb(C,N) precipitates during tensile testing at elevated temperatures. At 550 °C, no evidence of the formation of new precipitate is found. However, Cr enrichment at grain boundaries (GBs) is observed both the interrupted and failed samples (Fig. 13a and b) while slight Mo segregation to GB is found only in the failed sample (Fig. 13b). This may indicate that the mobility of Cr at 550 °C is already high enough to follow the dislocations with drag, thus DSA effect is observed until the sample fails. At 650 °C, in the interrupted sample no new precipitate is observed but Cr segregation at grain boundaries occurred (Fig. 13c). However, the formation of new precipitates at grain boundaries is found (Fig. 13d) in the failed sample. EDS analysis shows that the grain boundary precipitates are Cr-rich carbide. The formation of such carbides will lead to reduction in Cr content within the matrix and thus reducing the contraction of Cr atoms to pin mobile dislocations. As a consequence, the DSA effect is suppressed. This may be the reason that DSA phenomenon disappears after ~2.5% strain at 650 °C (Fig. 6). At 750 °C, even in the interrupted sample (only soaked for ~33 min), a continuous distribution of carbides has formed at grain boundary (Fig. 14), which also results in Cr depletion at grain boundaries and in the regions close to the carbides. EDS and selected area electron diffraction (SAD) pattern confirm that they are $M_{23}C_6$ (Fig. 14). The carbides grow into the matrix on one side, usually having a cube-to-cube orientation relationship (Fig. 14h). A previous study shows that $M_{23}C_6$ precipitates preferentially at GBs in short time during service at 600–1000 °C [24]. Sourmail observed the formation of $M_{23}C_6$ after very short aging times (e.g. 30 min) at 750 °C in a stabilized stainless steel [25]. The TTP curve of $M_{23}C_6$ in TP310 stainless steel exhibits a C-

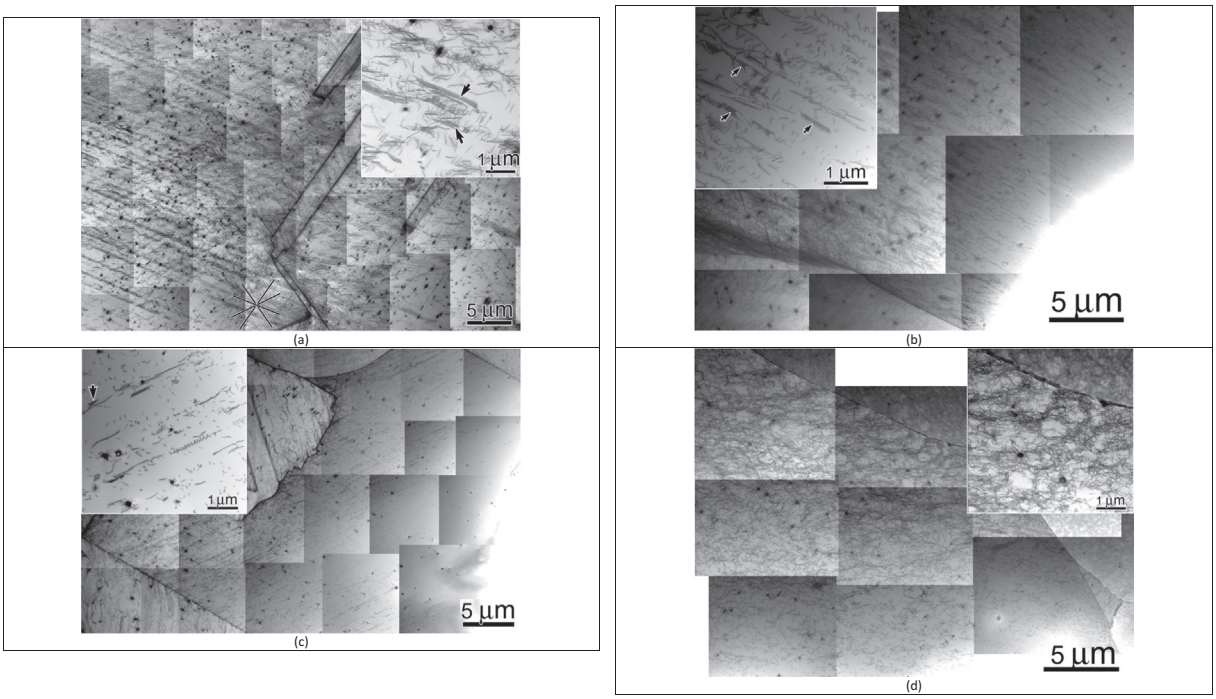

Fig. 9. BF-STEM images of the interrupted as-received samples at various temperatures were taken using multi-beam condition with beam directions (b.d.) of [101] for room temperature (four {111} slip traces marked on the image) (a), of [101] for 550 °C (b), of [101] for 650 °C (c) and of ~[101] for 750 °C (d). Notes: the insets to the each image are its corresponding image at higher magnification. Lamellae in Fig. 9a are annealed twins, black regions – Nb(CN), arrows in the insets - stacking faults, low density of dislocations is observed in the thin region (e.g. close to the holes).

shape with a nose temperature of ~750 °C [26]. These findings are in accordance with our observation of a continuous distribution of $M_{23}C_6$ on GBs in the interrupted tensile sample at 750 °C.

3.5. Fractography and failure mechanism

To better understand the underlying failure mechanisms of Alloy 709, the fracture surfaces of various samples along with their cross-sections are carefully examined. Overview of the fracture surfaces of the as-received samples tested at various temperatures is illustrated in Fig. 15a1–4, revealing a change in fracture surface appearance with testing temperature. A classic cup and cone morphology is observed at RT and 750 °C (i.e. no DSA regime), which exhibits two zones: the inner flat fibrous zone, where fracture initiates, and an outer shear-lip zone where final fracture takes place along 45° with the tension direction. In the DSA regime (i.e. 550 and 650 °C), the size of the fibrous zone reduces, especially at 550 °C compared to that at other temperatures. These observations are also evidenced by BSE images of the longitudinal cross-sectioned samples (Fig. 15c1–c4). Shear failure commonly leads to reduction in ductility. In contrast, no reduction in ductility is observed at 550 °C (Figs. 6 and 7). Further observation on the fracture surface reveals that the sample tested at 550 °C failed in a ductile mode (Figs. 15b2 and 16a). The surface consists of coarse dimples, which could be the result of voids nucleation at primary Nb(C,N) (Fig. 16a), and fine dimples, which could nucleate at small Nb(C,N) (Fig. 16a). Although some flat regions (arrowed in Fig. 15b2) are found at the fracture surface of samples tested at 550 °C, those regions are still covered by fine dimples as shown in Fig. 16a. Those observations at 550 °C suggest a ductile behaviour involving void nucleation, growth and coalescence. Alomari et al. [1] found that the enhanced ductility in DSA regime in Alloy 709 is related to negative strain rate sensitivity. When tested at other temperatures (i.e. RT, 650 and 750 °C), the fracture surfaces also show coarse and fine dimples similar to that observed in the samples tested at 550 °C. As in the sample tested at 550 °C, the coarse and fine dimples are associated with primary Nb(C,N) and fine Nb(C,N), respectively. An example showing a crack nucleated from primary Nb(C,N) is illustrated in Fig. 16b. However, Fig. 15b indicates that the number of coarse dimples increases with testing temperature except for 550 °C. The statistic results as listed in Table 2 show that the area fraction of coarse dimples increases up to 43% for the sample tested at 750 °C from 20% for those tested at RT. The mean diameter of these coarse dimples is about ~13 μm for the alloy tested at RT, about one order of magnitude larger than the primary Nb(C,N). This is because the dimples form as a result of the void nucleation at Nb(C,N), growth and coalescence. Furthermore, the void growth rate increases with increasing temperature. Therefore, more and bigger coarse dimples and thus higher volume fraction are expected to be observed in the samples tested at higher temperatures. Nevertheless, the sample tested at 550 °C shows the smallest area fraction of coarse dimples. This may be because the nucleation of voids at Nb(C,N)/matrix interface results from the interaction of dislocations and Nb(C,N) particles, and the probability of this interaction is relatively low due to the inhomogeneous planar deformation at 550 °C.

To understand the influence of aging on ductility and failure mechanism, the fracture surfaces of the aged samples are also studied in detail, and illustrated in Fig. 17. A large amount of secondary cracks along grain boundaries are observed in the aged sample tested at RT (Fig. 17b1). This suggests that the failure primarily follows on grain boundaries. Examination on the longitudinal section of the fractured testpieces also indicates that the failure is correlated with the grain boundaries (Fig. 18). Closely examination shows the fracture surface is still covered with microvoids, as seen in Fig. 18c. However, they are shallower and far underdeveloped compared with those in the as-received samples. Intergranular failure at RT could be attributed to the following reasons: aging (at 650 °C for 2000 h) brings about a continuous distribution of carbides on grain boundary (Fig. 4), the brittle carbides could not accommodate any deformation thus resulting in cracking (Fig. 18b),

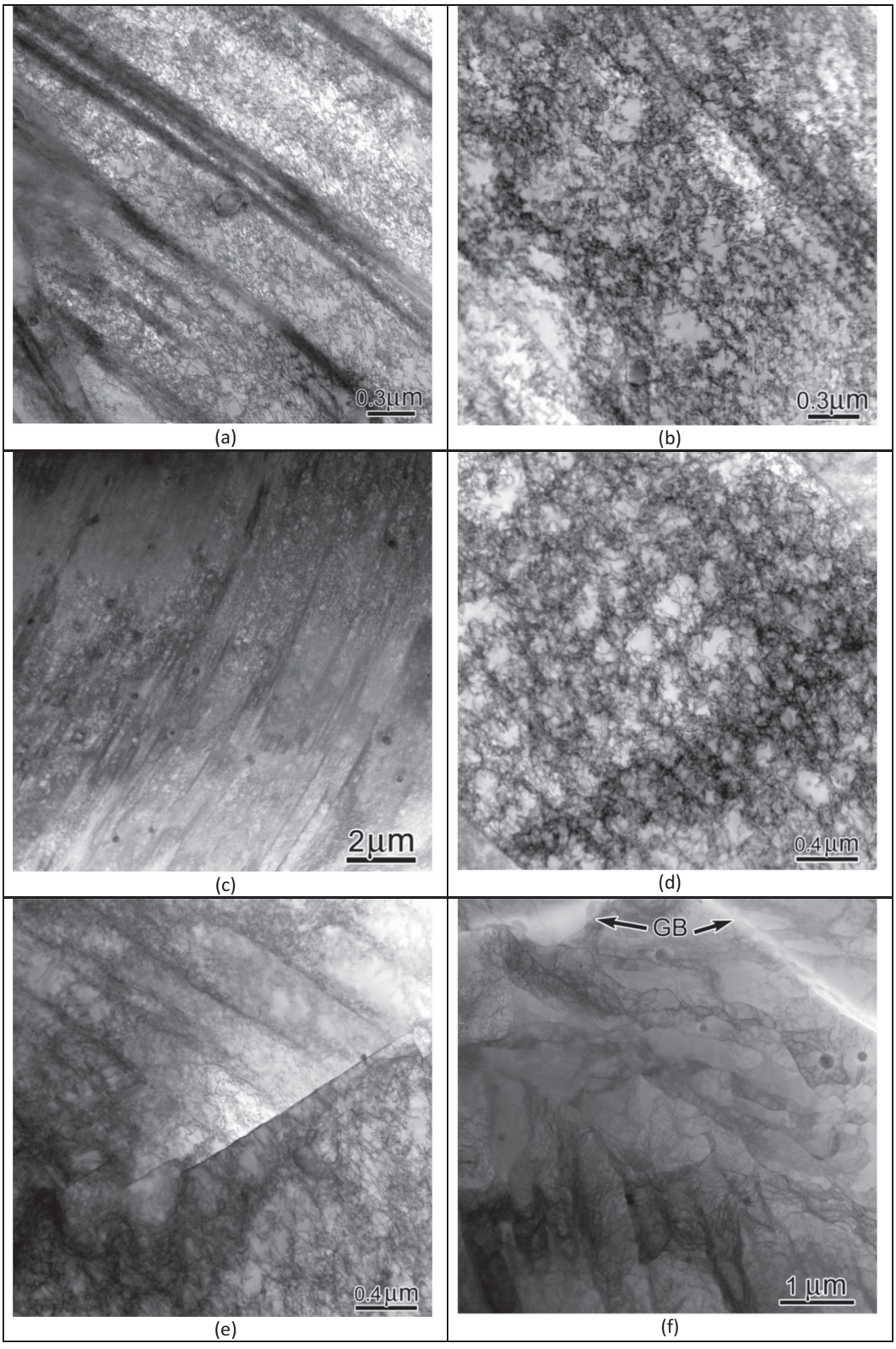

Fig. 10. BF-STEM images from the as-received samples strained to failure at RT (a and b), 550 °C (c), 650 °C (d and e) and 750 °C (f).

and the cracks further propagate easily through grain boundary by linking of fractured carbides. Therefore, the synergistic effect of intergranular failure path and formation of shallow microvoids makes the aged sample have 30% elongation at RT, which is reduced by 30% compared to that in the as-received sample (40% elongation). With increasing test temperature, the carbides appear somewhat ductility, and are able to accommodate some strain, thus leading to reduction in the number of secondary cracks (Fig. 17b). The fracture surface also shows that the aged sample tested at 750 °C appears clearly necking (Fig. 17a3), which is attribution to

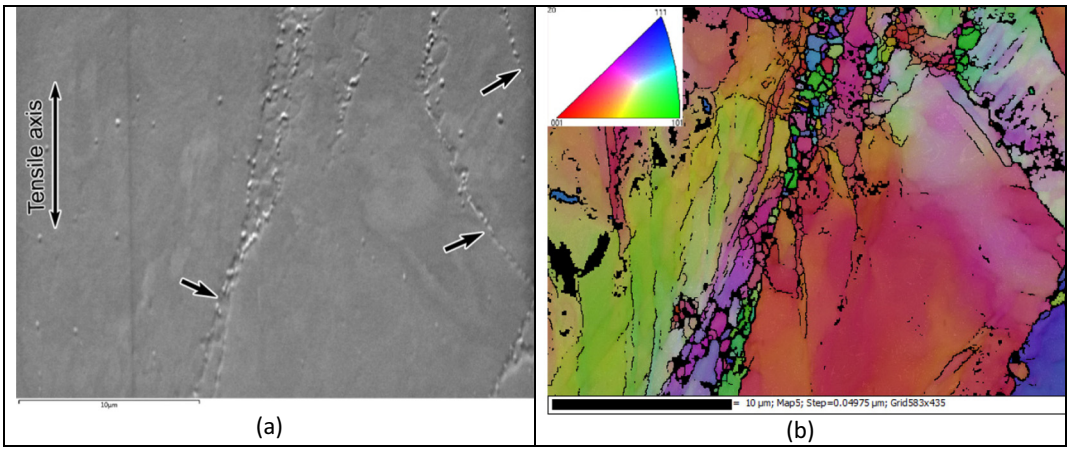

Fig. 11. SEM image taken from the longitudinal section of the fractured sample tested at 750 °C (a) and its corresponding grain orientation colour maps overlaid with grain boundary distribution (b). Note: prior grain boundaries are depicted by the arrows in Fig. 11a.

the enhancement of DRX induced by precipitates, as mentioned in Section 3.3.

4. Discussion

Tensile testing shows that, although UTS obviously decreases with increasing temperature, the yield strength has almost no change in the testing temperatures range from 550 to 750 °C, and the flow stress in the strain range of ~8% to ~15% at 650 °C is slightly higher than that at 550 °C. Aging leads to increment in yield strength but reduction in UTS and ductility. These interesting observations could be associated with deformation mechanism and the evolution of precipitates during high temperature testing.

4.1. Influence of temperature on mechanical response of the as-received samples

Due to the presence of alloying elements, the stacking-fault energy (SFE) in austenitic steels is usually low and as a consequence the dissociation distance between Shockley partial dislocations is large. Thus, the dislocations in the virgin state of material prefer to be present in planar form (e.g. individual dislocations, stacking faults, pile-ups [27,28]), as shown in Figs. 3a and 9. At room temperature, under onset of plastic strain (e.g. the interrupted sample of ~2% strain), the dislocation density increase significantly (Fig. 9a), thus the material shows high strain-hardening. Low SFE restricts cross-slip of dislocations and thus dislocation movement is limited to planar slip (Fig. 9a). As a result, with further straining, slip on the critical plane prevails, leading to further localisation on this plane (Fig. 10a). Additionally, with the increase in plastic strain, the dislocations multiply continuously and dislocation interaction becomes complicated and more tangled (Fig. 10b). This observation has been well documented in the literature [29,30]. As the total dislocation density tends to reach its equilibrium state and remains almost constant after achieving a maximum, the material shows maximum flow stress. With the acceleration on annihilation of dislocation via interaction with opposite sign dislocations, the material becomes softer, thus leading to necking.

As the testing temperature rises from RT to 550 °C, the effect of solid solution strengthening become less significant and thermally activated processes allow the relaxation of stresses. As a result, the material shows lower yield strength and strain-hardening rate at onset of plastic strain than those tested at room temperature. Nevertheless, the cross-slip of dislocations is still difficult at 550 °C, thus the dislocations still appear in planar forms (e.g. slip bands, stacking faults) (Fig. 9b). Additionally, the diffusivity of interstitial and substitutional atoms increases significantly at 550 °C, which is proved by the segregation of Cr to grain boundary in the interrupted sample (Fig. 13a). This means that the solute atom of Cr is capable of diffusing to dislocations to impede its movement, thus producing DSA effect and causing a serrated flow stress (Fig. 6). The solute atoms pinning dislocation movement inevitably increase the flow stress and thus strain-hardening (Fig. 8). As a consequence, the clear softening (necking) observed in the sample tested at RT, was not found in the sample tested at 550 °C (Fig. 6). The DSA effect often leads to planar arrangement of dislocations and localised deformation, thus more band-like features (Fig. 10c) and the shear failure (Fig. 15c2) are observed at 550 °C.

As testing temperature increases to 650 °C, at low strain, the Alloy 709 still deforms prominently via planar forms (e.g. slip bands and stacking faults) (Fig. 9c), and the solute atoms still can drag dislocation movement but the ability of drag alleviates due to higher mobility of the solutes compared to that at 550 °C, thus decreasing the amplitude of serration (Fig. 6b). However, the formation of Cr-rich carbides at grain boundary (Fig. 13d) definitely leads to reduction in concentration of the solute (Cr) atoms to pin dislocations. As a result, the DSA effect is suppressed with further straining. On the other hand, GB carbides inevitably restrict GB motion, thus increasing the flow stress. This could be the reason for higher flow stress than that at 550 °C in the strain range of ~8% to ~15% (Fig. 6a). With temperature increased to 650 °C, the cross-slip becomes easier and interaction of dislocations occurs frequently, eventually with further increasing deformation dislocation cells form (Fig. 10d). This could improve plasticity. In contrast, no increased ductility is observed compared to the tests at lower temperatures. This could be attributed to the formation of carbides at GBs, because the precipitation of carbides at GBs is well known to decrease the plasticity and ductility of austenitic stainless steels [31,32].

At 750 °C, the mobility of solute is high enough to follow the dislocations without any drag or disruption, thus no serrated flow is observed (Fig. 6). Additionally, with increasing temperature the activity of dislocations seriously improves and dislocation interaction is clearly alleviated, thus the Alloy 709 shows lowest strain-hardening at 750 °C. However, the formation of a nearly continuous distribution of $M_{23}C_6$ on GBs at the initial stage of testing (Fig. 14) will impede the transmission of dislocations through the GBs, which increases consequently the strength of the Alloy 709. This could be the reason that the flow stress at onset of plastic

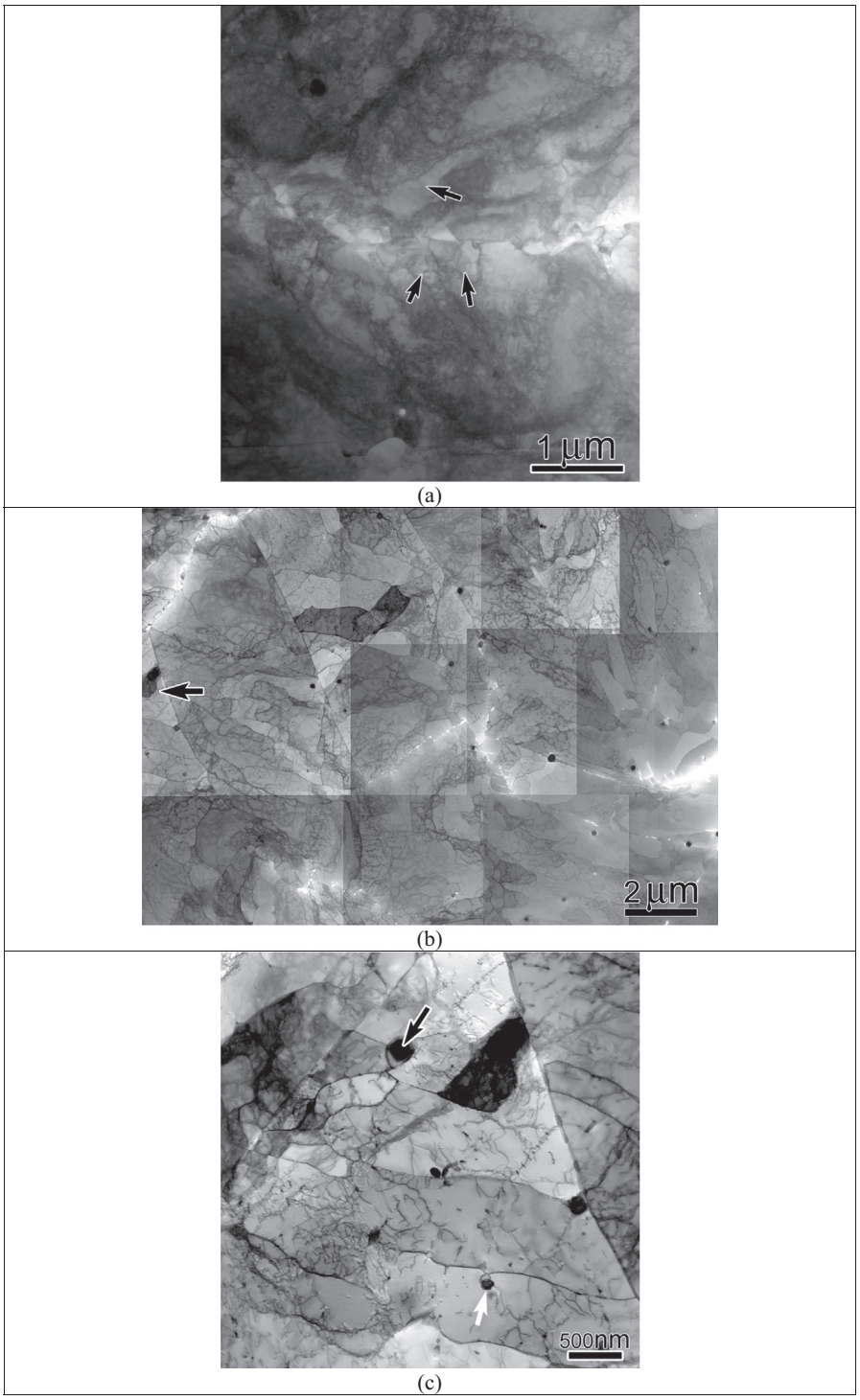

Fig. 12. BF-STEM images from the aged samples strained to failure at 650 °C (a) and 750 °C (b and c). Note: the arrows in Fig. 12a – subgrains, the arrow in Fig. 12b – the region where Fig. 12c was taken from, the dark arrow in Fig. 12c – large particle acting as DRX nucleation site, and the white arrow in Fig. 12c – the particle pinning the boundary.

deformation at 750 °C does not decrease clearly compared with that at 550 and 650 °C (Figs. 6 and 7). The ability to cross-slip of dislocations in fcc crystals could be highly enhanced at temperatures close to 700 °C [33]. It is, therefore, expected that the cross-slip of dislocations and probably climb will become the main deformation modes at 750 °C. As a result, the tangled dislocations and cell-like structures are observed even in the early stage of straining, e.g. in interrupted sample (Fig. 9d). Further straining promotes the process of dynamic recovery and probably recrystallization, which makes the material become softer, thus leading to necking (Fig. 6). The formation of subgrains via dynamic recovery is observed at 750 °C (Fig. 10f) but not at 650 °C, which is because diffusion-controlled thermal recovery is strongly temperature dependent. The observation of subgrains indicates that dislocation climb is rate controlled. The work of Blum and his co-authors [34,35] show that, if enough strain is accumulated, subgrain formation will eventually

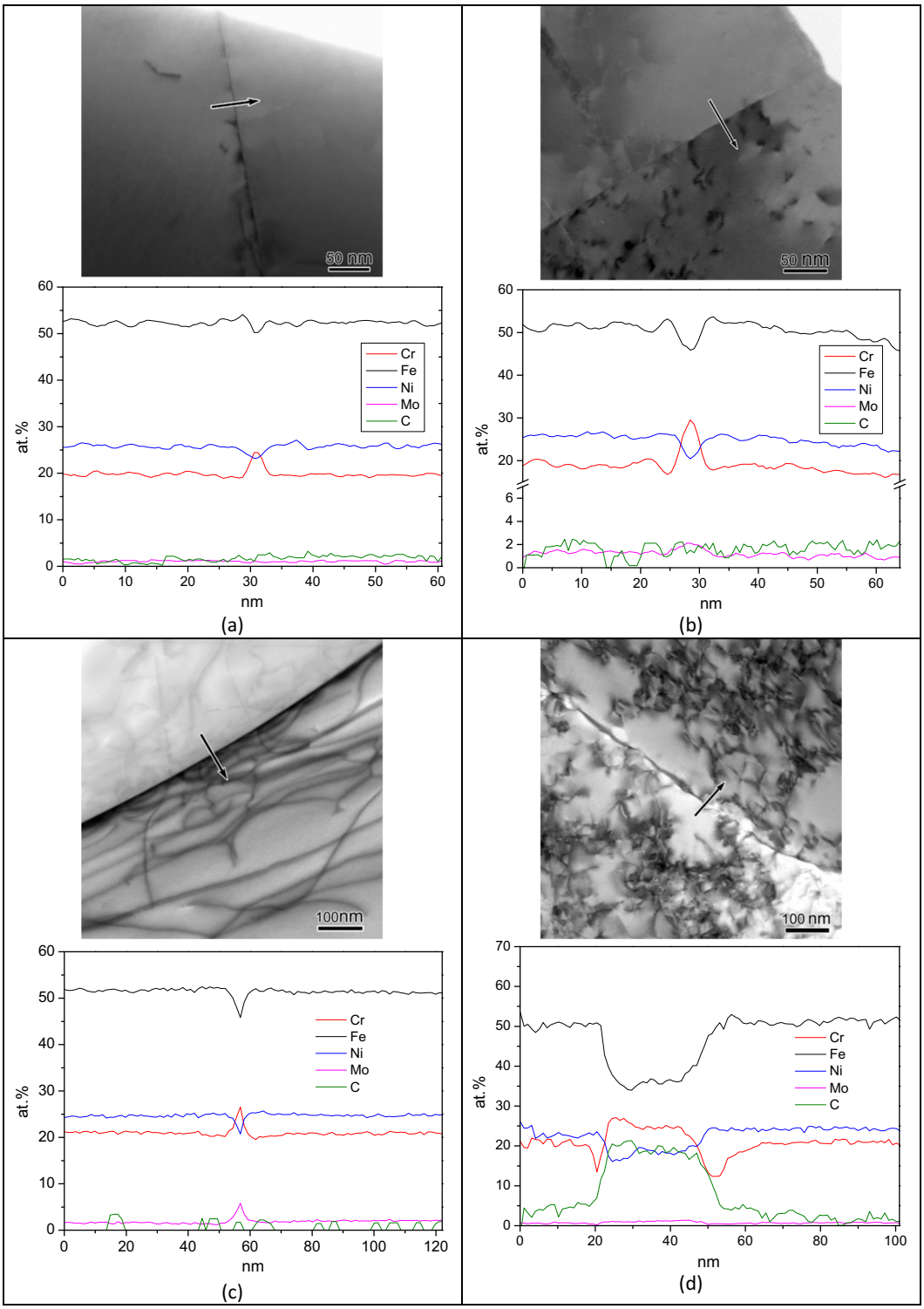

Fig. 13. BF-STEM images and EDS line scans across the grain boundaries and the particle on the grain boundaries from: the interrupted (a) and failed (b) samples at 550 °C showing Cr segregation at the grain boundary, and the interrupted sample at 650 °C revealing the segregation of Cr and Mo to the grain boundary (c) and the failed sample at 650 °C illustrating the formation of Cr-rich carbides at the grain boundary (d).

always occur in a single-phase material, and that the size of the subgrains is then temperature- and stress- dependent quantity.

4.2. Influence of aging on strength

Higher yield strength observed in the aged Alloy 709 is attributed to aging process at 650 °C, which strongly affects the specific contributions of solid solution strengthening and dispersion strengthening to the total strength. Furthermore, since the aging at 650 °C did not change the grain size, we can conclude with confidence that the change in the strength is not related to the grain size. Aging leads to the formation of particles at both the grain boundaries and interior of grains, especially on dislocations as a unique reinforcement factor. Although the formation of particles

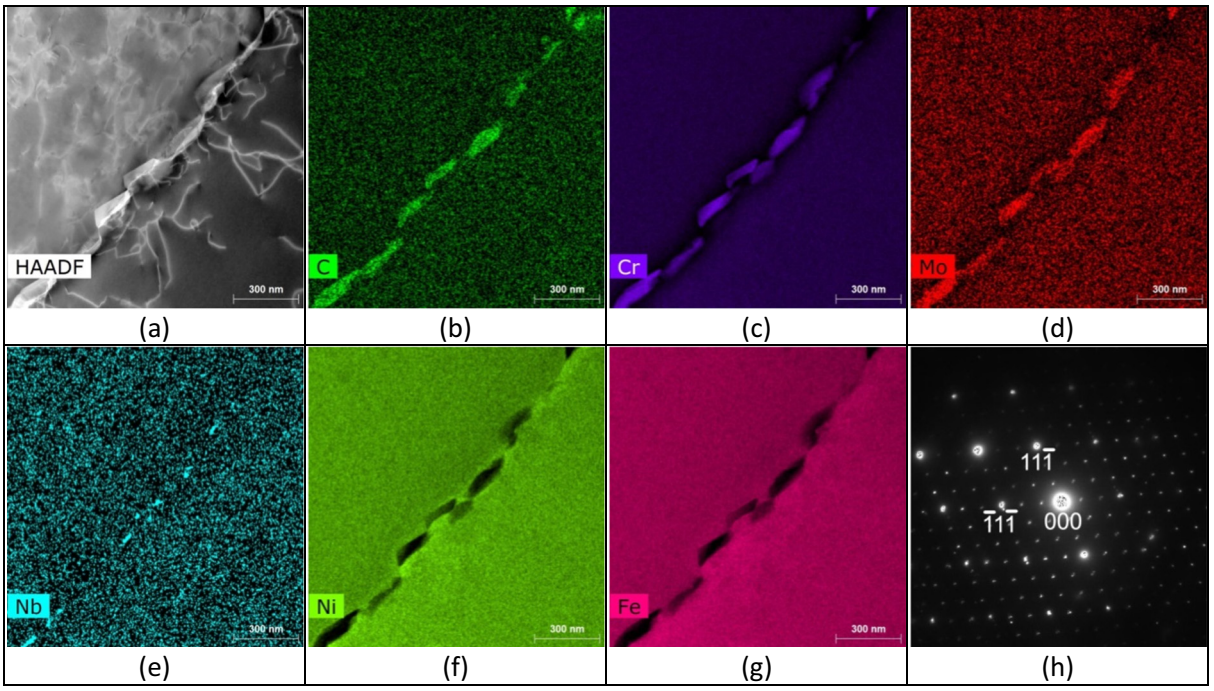

Fig. 14. HAADF-STEM image showing a continuous distribution of particles on the grain boundary in the interrupted sample at 750 °C (a), EDS maps for the grain boundary particles (b–g), and selected area electron diffraction patterns from the matrix along [011] direction and a grain boundary particle ($M_{23}C_6$) along [011] direction (h) showing an orientation relationship between $M_{23}C_6$ and matrix. Note: intensive spots from matrix and weak spots from $M_{23}C_6$.

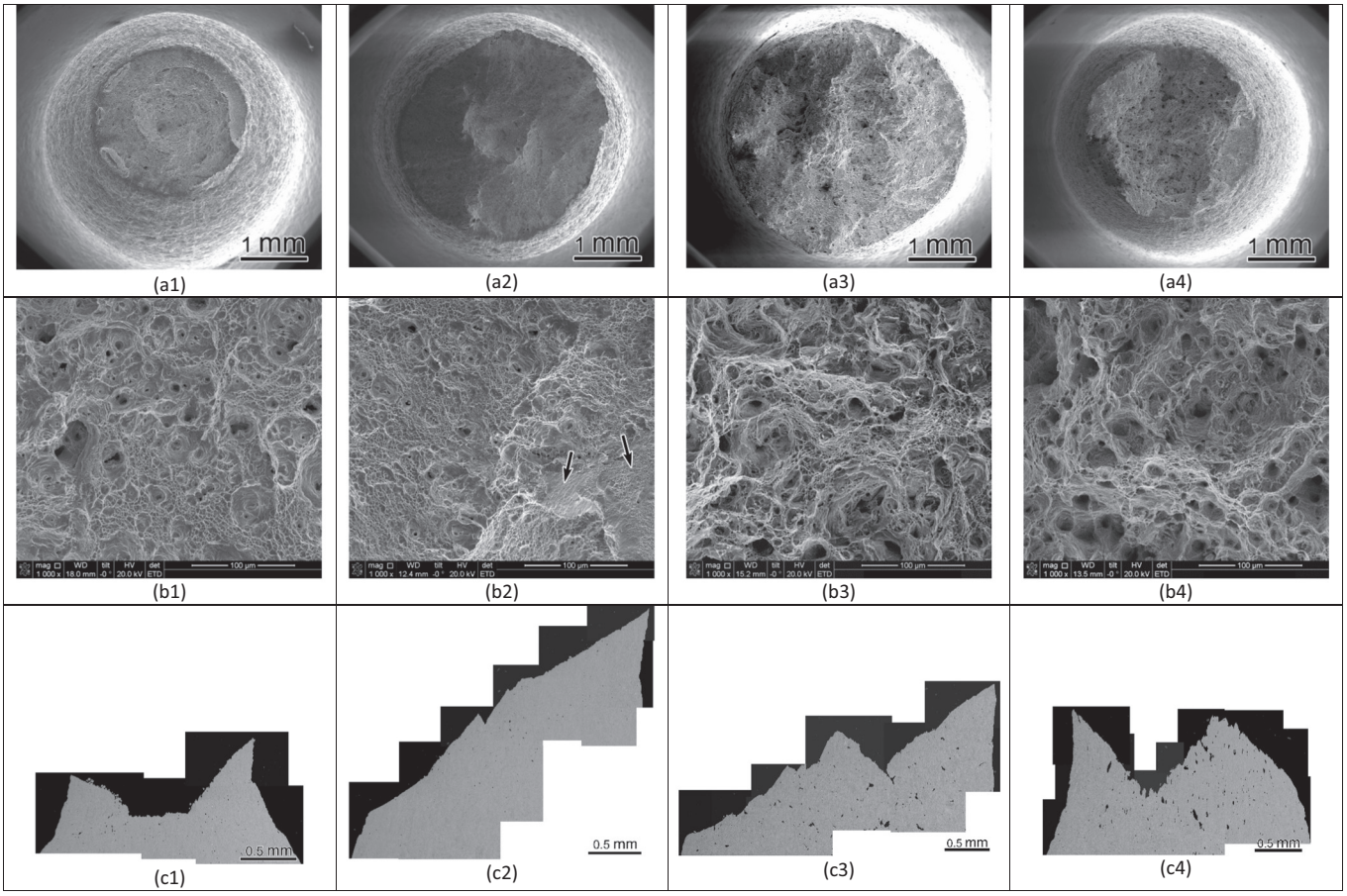

Fig. 15. Fractography analysis on fracture surfaces of the as-received samples at low (a) and high (b) magnification and the longitudinal cross-sectioned samples (c) at different temperatures of (1) RT, (2) 550 °C, (3) 650 °C and (4) 750 °C.

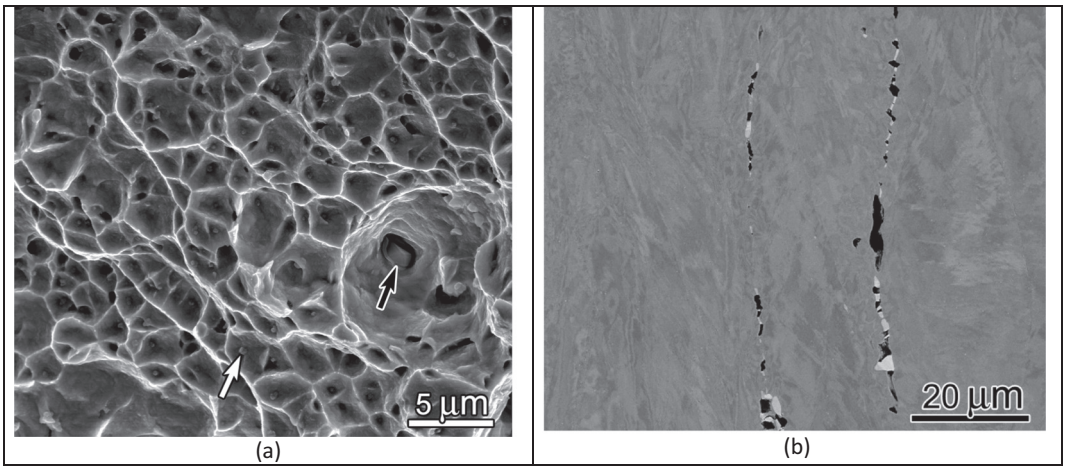

Fig. 16. Two types of dimples: coarse dimple associated with primary carbonitride (black arrow) while fine dimple related to fine NbCN (white arrow) (a), and BSE image of the cross-sectioned sample showing cracking associated with primary carbonitrides (b).

(e.g. Cr-rich carbide) evidently decreases the solubility of Cr and C in the matrix, thus reducing solid solution strengthening induced by Cr and C, the tensile testing has confirmed that this reduction is much smaller compared with increment in the strength produced by precipitate strengthening. The strengthening induced by precipitates (σ_p) is due in part to the creation of Orowan loops (Orowan strengthening) which may be estimated from the following equation.

$$\sigma_p = \mu b/2\lambda \quad (1)$$

where μ is the shear modulus, *b* is the Burgers vector and λ is the mean planar square lattice spacing.

For 'significant' strengthening by this mechanism, $\sigma_p/\mu > 10^{-3}$ is a reasonable requirement. Taking furthermore $\lambda = (\pi/6)df^{-1/2}$ (*d* is the dispersoid diameter and *f* is the dispersoid volume fraction) [36], it is easily seen that a particle radius < 100 nm is required for a dispersoid volume fraction to assume practical significance. Although the volume fraction and size of the precipitates (carbides and *Z*-phase) have not been quantified here, those fine Z-phase (with size of several nanometers) sitting on dislocations can effectively pin mobile dislocations, thus increasing the strength. It is, herein, not unreasonable to assume that the strengthening induced by Z-phase has a major contribution to increment the yield strength. Furthermore, the appearance of $M_{23}C_6$ on grain boundary impedes the motion of GBs, thus increasing the strength of material [37]. Therefore, the yield strength induced by aging could result from dispersoid strengthening and the precipitation of $M_{23}C_6$ at GBs. During plastic deformation, the precipitates, especially Z –phase, could act as obstacles to dislocation movement (Fig. 19), thus leading to a higher strain-hardening than that in the as-received samples at the onset of plastic deformation (Figs. 6 and 8). Further straining generates more dislocations, which pile up around the precipitates and grain boundary. This brings about accumulated stress/strain at the interface of $M_{23}C_6$ and grain boundary. Unfortunately, $M_{23}C_6$ is a brittle phase and has low $M_{23}C_6$ – matrix bond strength [38], thus $M_{23}C_6$ cannot accommodate strain, which causes inevitably $M_{23}C_6$ phase cracking and the formation of microcracks at $M_{23}C_6$/grain boundary interface (Fig. 18b). This evidently leads to the rapid drop of strain-hardening with increasing strain (Fig. 8). The cracks further propagate easily through grain boundary by linking of fractured carbides or voids formed by decohesion of carbides with GB, leading to an intergranular failure mode (Fig. 17b1), hence the aged Alloy 709 shows lower elongation and UTS compared to its counterpart (Figs. 6 and 7).

Table 2
Volume fraction (V), equivalent diameter (d) of coarse and fine dimples of the as-received alloy at different testing temperatures.

	Coarse dimples		Fine dimples	
	V (%)	d (μm)	V (%)	d (μm)
RT	20 ± 5	13 ± 7	80 ± 5	1.2 ± 0.4
550 °C	13 ± 4	10 ± 4	87 ± 4	1.0 ± 0.3
650 °C	38 ± 6	15 ± 6	62 ± 6	1.1 ± 0.3
750 °C	43 ± 5	17 ± 8	57 ± 5	1.2 ± 0.3

5. Conclusions

The tensile response of the Alloy 709 in the as-received and aged (at 650 °C for 2000 h) conditions, along with deformation microstructure and fracture mechanism, at temperatures ranging from RT to 750 °C have been studied. The following conclusions could be drawn from this work:

1. DSA effect was observed at 550 °C in both as-received and aged materials. However, at 650 °C this effect was found only in the as-received sample in a limited strain range of 1.2%–2.5%. This could be related to reduction in Cr content inside the grains due to the formation of Cr-rich carbide at GBs during testing for the as-received material at 650 °C.
2. For the as-received material, the yield strength reduces with increasing temperature. At the temperature range of 550–750 °C, however, no clear reduction in the yield strength is found, which could be associated with the formation of $M_{23}C_6$ during tension testing at 650 and 750 °C. Higher strain-hardening rate was observed at 550 °C than that at RT, which is correlated with the DSA effect. At 750 °C the elongation increases clearly due to the dynamic recovery and recrystallization.
3. Aging increases the yield strength at all testing temperatures, which is contributed to dispersoid strengthening induced by $M_{23}C_6$ and Z-phase. Reduction in the ultimate tensile strength and ductility is due to the formation of brittle $M_{23}C_6$ at grain boundaries.

CRediT authorship contribution statement

Rengen Ding: Investigation, Writing - original draft, Writing - review & editing. **Jin Yan:** Investigation, Writing - review & editing. **Hangyue Li:** Investigation, Writing - review & editing. **Suyang Yu:** Investigation, Writing - review & editing. **Afsaneh Rabiei:** Funding acquisition, Writing - review & editing. **Paul Bowen:** Funding acquisition, Writing - review & editing.

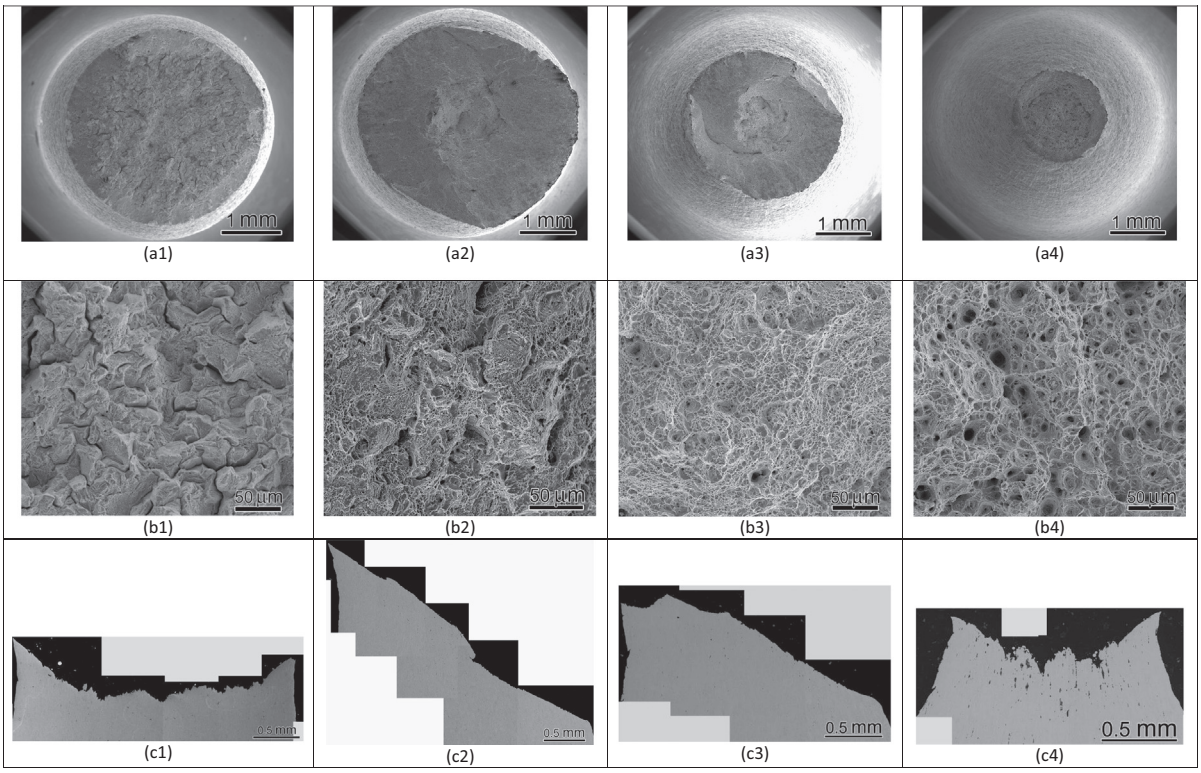

Fig. 17. Fractography analysis on fracture surfaces of the aged samples at low (a) and high (b) magnification and the longitudinal cross-sectioned samples (c) at different temperatures of (1) RT, (2) 550 °C, (3) 650 °C and (4) 750 °C.

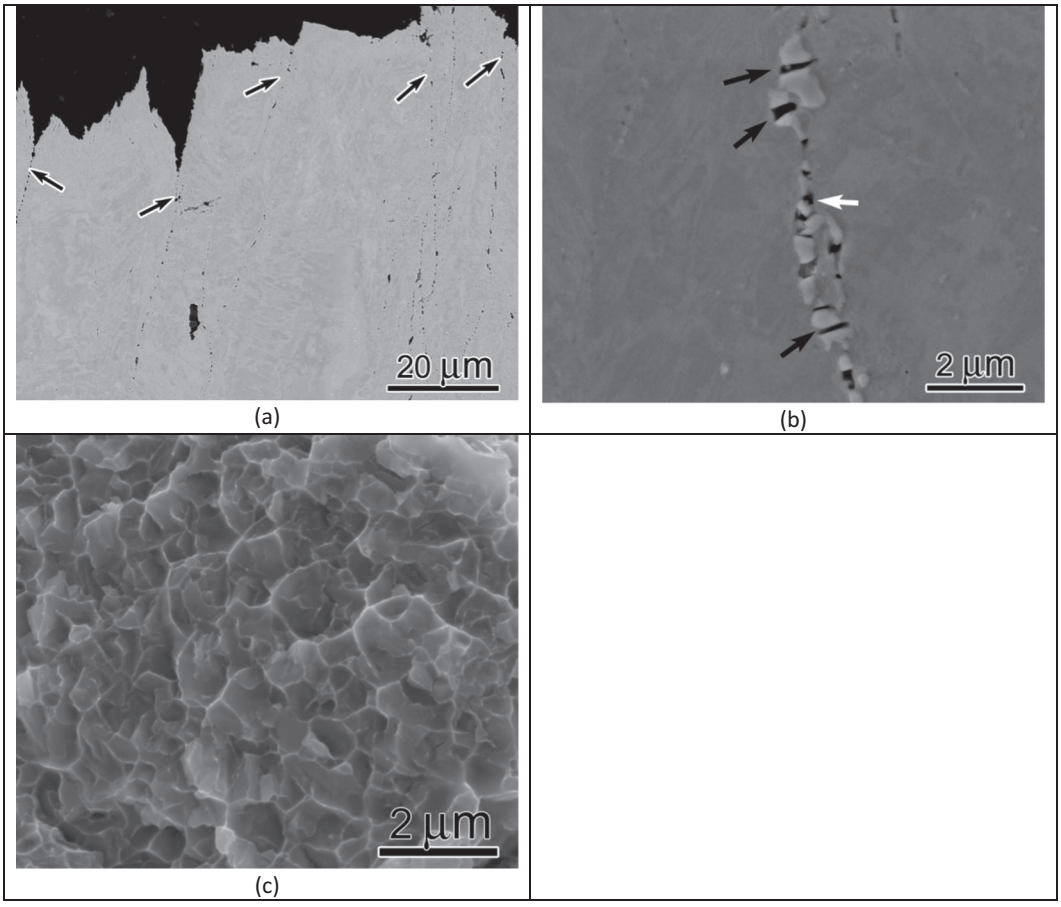

Fig. 18. BSE image of the cross-sectioned sample tested at RT showing cracking associated with the grain boundaries (arrowed) (a), higher magnification image revealing the big particles broken (arrowed in black) while the voids formed along the interface of small particle and matrix (arrowed in white) (b), and higher magnification of Fig. 17b1 exhibiting fine dimples (c).

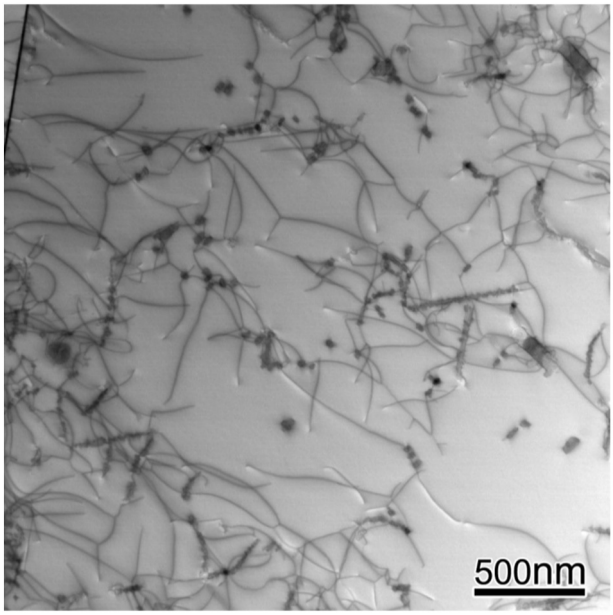

Fig. 19. BF-STEM image of the interrupted aged sample at 750 °C was taken using multi-beam condition at beam direction of ~[101], showing some of dislocations are pinned by Z-phases (black dots).

Acknowledgments

This study is part of a project funded by Research Council of United Kingdom (RCUK) award number EP/N016351/1 and the United States of America's Department of Energy (DOE) nuclear energy university program (NEUP) award number 2015-1877/DE-NE0008451. We thank Prof. Ian Jones for useful discussions.

References

[1] A.S. Alomari, N. Kumar, K.L. Murty, Mater. Sci. Eng. A 729 (2018) 157.
[2] S. Upadhayay, H.Y. Li, P. Bowen, A. Rabiei, Mater. Sci. Eng. A 733 (2018) 338.
[3] S.Y. Yu, J. Yan, H.Y. Li, R. Ding, A. Rabiei, A. Lall, P. Bowen, Mater. Sci. Eng. A (2019).
[4] S. Byun, N. Hashimoto, K. Farrell, Acta Mater. 52 (2004) 3889.
[5] H.X. Pei, H.L. Zhang, L.X. Wang, S.L. Li, D.Z. Li, X.T. Wang, Mater. High Temp. 31 (2014) 198.
[6] D.J. Michel, J. Moteff, A.J. Lovell, Acta Metall. 21 (1973) 1269.
[7] B.K. Choudhary, J. Christopher, Mater. Sci. Eng. A 651 (2016) 486.
[8] X. Feaugas, H. Haddou, Metall. Mater. Trans. A 34 (2003) 2329.
[9] A. Kisko, R.D.K. Misra, J. Talonen, L.P. Karjalainen, Mater. Sci. Eng. A 578 (2013) 408.
[10] T. Sourmail, H.K.D.H. Bhadeshia, Metall. Mater. Trans. A 36 (2005) 23.
[11] B.K. Choudhary, E. Isaac Samuel, K. Bhanu Sankara Rao, S.L. Mannan, Mater. Sci. Technol. 17 (2001) 223.
[12] R. Ding, Jin Yan, Hangyue Li, Suyang Yu, Afsaneh Rabiei, Paul Bowen, Microstructural evolution of Alloy 709 during aging, submitted to J. Microstruct. Charact. (2019).
[13] C. Fressengeas, A.J. Beaudoin, M. Lebyodkin, L.P. Kubin, Y. Estrin, Mater. Sci. Eng. A 400–401 (2005) 226.
[14] M.A. Soare, W.A. Curtin, Acta Mater. 56 (2008) 4091.
[15] K. Gopinath, A.K. Gogia, S.V. Kamat, U. Ramamurty, Acta Mater. 57 (2009) 1243.
[16] G.W. Han, I.P. Jones, R.E. Smallman, Acta Mater. 51 (2003) 2731.
[17] Y. Koizumi, T. Nukaya, S. Suzuki, S. Kurosu, Y. Li, H. Matsumoto, K. Sato, Y. Tanaka, A. Chiba, Acta Mater. 60 (2012) 2901.
[18] J.P. Hirth, J. Lothe, Theory of Dislocations, Wiley, New York, 1981 857.
[19] E.I. Samuel, B.K. Choudhary, K. Bhanu Sankara Rao, Scr. Mater. 46 (2002) 507.
[20] W. Karlsen, M. Ivanchenko, U. Ehrnstén, Y. Yagodzinskyy, H. Hänninen, J. Nucl. Mater. 395 (2009) 156.
[21] A. Rollet, F. Humphreys, G.S. Rohrer, M. Hatherly, Recrystallisation and Related Annealing Phenomena, Second ed. Elsevier Ltd, 2004.
[22] R.D. Doherty, D.A. Hughes, F.J. Humphreys, J.J. Jones, D.J. Jensen, M.E. Kassner, W.E. King, T.R. McNelley, H.J. McQueen, A.D. Rollet, Mater. Sci. Eng. A 238 (1997) 219.
[23] E. Nes, Acta Metall. 24 (1976) 253.
[24] A.F. Padilha, P. Rios, ISIJ Int. 42 (2002) 325.
[25] T. Sourmial, Mater. Sci. Technol. 17 (2001) 1.
[26] W. Binder, C. Brown, R. Franks, Trans. Am. Soc. Met. 41 (1949) 1301.
[27] V. Gerold, H.P. Karnthaler, On the origin of planar slip in f.c.c. alloys, Acta Metall. 37 (1989) 2177.
[28] K. Obrtlík, T. Kruml, J. Polák, Dislocation structures in 316L stainless steel cycled with plastic strain amplitudes over a wide interval, Mater. Sci. Eng. A 187 (1) (1994).
[29] J. Polák, R. Petráš, M. Heczko, T. Kruml, G. Chai, Evolution of the cyclic plastic response of Sanicro 25 steel cycled at ambient and elevated temperatures, Int. J. Fatigue 83 (2016) 75.
[30] M. Heczko, T. Kruml, J. Polák, Mater. Sci. Eng. A 680 (2017) 168.
[31] L.G. Zhang, X.Q. Hu, X.H. Kan, D.Z. Li, Mater. Des. 78 (2015) 42.
[32] D.R. Hu, G. Bai, J. Li, J. Zhang, T. Zhang, H. Fu, Mater. Sci. Eng. A 548 (2012) 83.
[33] D. Caillard, J.L. Martin, Thermally Activated Mechanisms in Crystal Plasticity, Pergamon, Amsterdam, Boston, Mass, 2003.
[34] Y. Qin, G. Gotz, W. Blum, Mater. Sci. Eng. A 341 (2003) 211.
[35] R. Sedla˘cek, W. Blum, J. Kratochvil, S. Forest, Metall. Trans. A. 33 (2002) 319.
[36] A.J. Röslerlom, M. Bäker, Acta Mater. 48 (2000) 48.
[37] J.S. Zhang, P.E. Li, J.Z. Jin, Acta Metall. Mater. 39 (1991) 3063.
[38] J. Larson, Metall. Trans. A. 7 (1976) 1497.